Hybrid mineral-bonded protective layers for enhanced self-centering capacity of reinforced concrete beams subjected to blast

Franz Bracklow [a], Christopher M. Jackson [b], Cesare Signorini [c],*, Eric Jacques [b], Birgit Beckmann [a], Manfred Curbach [a], Viktor Mechtcherine [c]

[a] *Institute of Concrete Structures, TU Dresden, 01062 Dresden, Germany*
[b] *Department of Civil and Environmental Engineering, Virginia Polytechnic Institute and State University, 24061 Blacksburg, VA, USA*
[c] *Institute of Construction Materials, TU Dresden, 01187 Dresden, Germany*

ABSTRACT

With the aging of infrastructure and the threat of terrorist attacks and military actions worldwide, there is a need to develop retrofits for critical infrastructure, which is often made of reinforced concrete. While it is paramount that these retrofits enhance robustness of structural members so that structural elements remain operable, it is also desired that they show minimal signs of significant plastic deformation (self-centering) and reduce spalling and fragmentation. Mineral-bonded composites with textile and/or short, dispersed fiber reinforcement are one such solution to provide existing structural elements with additional resistance and resilience. To determine the improvements provided by the devised retrofitting strategies, four reinforced concrete beams were constructed and tested in a shock tube research facility under a series of progressively higher blast loads. The results of these tests show that retrofits featuring either textile reinforcement or hybrid reinforcement (i.e., a combination of textile and short dispersed fibers) have a strong self-centering capability, even in situations where reinforced concrete beams would fail. In addition, single-degree of freedom analytical simulations are performed to highlight the predictive capabilities of the method and the accuracy of the calculated sectional capacity of the beams.

1. Introduction

The vast majority of reinforced concrete (RC) structures built over the last century lack adequate design to maintain their functionality and robustness under extreme loads, such as those caused by human activities (war, terrorism, accidental explosions) and natural disasters (earthquakes, floods, etc.). However, retrofitting existing structures for blast resilience poses significant challenges, as it requires adapting structures that were originally constructed with inadequate reinforcement, poor materials, and/or insufficient load paths to withstand high intensity, short duration blast loading [1,2]. Typical retrofitting techniques implemented to mitigate blast hazards in concrete structures can be broadly categorized into several approaches, including increasing the stand-off distance to reduce the intensity of the blast load; enhancing the strength of the component, often at the expense of reduced ductility; improving the ductility and energy absorption through by increasing the inelastic deformation capacity; and increasing the mass of structures to improve response in the high-impulse loading regime [3]. Recently, Johnson et al. [4,5] applied the self-centering principles, namely the ability of a structural element to return to its original

shape, in seismic engineering, and demonstrated that hybrid internal reinforcements, i.e. fiber reinforced polymer (FRP) and steel rebar, promote a self-centering effect in blast-loaded components. Indeed, while the FRP reinforcement was shown to provide an internal restoring force that tended to return the structures to their original position after the inertial loads were removed, the inelastic response of the steel reinforcement and concrete provided energy dissipation. While such hybrid reinforced concrete construction has been shown to benefit the performance and reduce the overall damage of RC members under blast loading, the concept of blast self-centering has yet to be demonstrated as a retrofit technique for blast resistant and resilient construction.

The most widely used retrofitting technique to enhance the blast performance of an existing structure is the application of an externally bonded or mechanically fastened strengthening layer [6]. The main advantages of applying external strengthening materials lie in their versatility, efficiency, customizable design, and high specific strength while adding minimal additional weight to the existing structure [7–9]. For far-field blast loads, which tend to activate bending and diagonal tensile shear modes, externally bonded FRPs are particularly advantageous because the fiber orientation and composite layout design can be

easily tuned to address these specific stress conditions. Many studies have focused on the strengthening potential of FRPs that incorporate high performance synthetic textiles as load-bearing elements in polymeric resins, that act as load-transmitting media [10,11].

Experimental results on the response of concrete slabs subjected to blasts highlight the convenience of externally bonded FRP in compensating for the intrinsic brittleness of RC members by significantly mitigating damage and deflections, especially when applied on both sides of the structural member [12]. FRP jackets can significantly increase the residual axial capacity of RC columns after a blast event [13]. Jacques et al. [14] showed that the use of glass FRP strips for both longitudinal and transverse jacketing of RC beams provided additional strength to the beam, in addition to preventing concrete spalling due to the tight confinement provided by the FRP jacketing. Remarkably, the improved elastic response of the retrofitted elements is critical in mitigating the detrimental effects of cyclic loading on the stiffness and load-bearing capacity of the structural member. However, a notable drawback of FRP materials is their linear elastic behavior and brittle failure. In addition, the use of FRPs for strengthening can introduce new, undesirable behaviors into structures, including debonding [15], load reversal failure [16], and vulnerability of the polymeric resins to thermal loads [17]. In addition, since FRPs behave elastically, the energy dissipation capacity of a retrofitted component is usually less than that of the original structure. This is antithetical to the current structural design philosophy of new buildings, where the goal is to develop significant plastic deformation for energy dissipation [18–20].

Mineral-bonded composites applied externally in thin layers represent a promising alternative to externally bonded FRP composites for blast strengthening applications. Following the successful example of FRPs, the use of textile-reinforced concrete (TRC), generally framed in the broader family of textile-reinforced cementitious composites, as thermally stable class of protective materials has gained popularity in recent decades. High-tenacity textiles embedded in cement-based materials lead to an improved global bending response, due to their in-plane membrane effect when subjected to dynamic loading. However, it has been demonstrated that the highest reinforcement potential is only guaranteed if the embedding medium features sufficient ductility and damage tolerance to immediately absorb the mechanical energy associated with dynamic loading such as impact or blast. While these textiles can improve the energy dissipation of such structures, they are unable to prevent spalling of the concrete matrix. In this regard, the use of fiber-reinforced matrices with pseudo-ductile behavior (e.g., strain-hardening cement-based composites, SHCC) is strongly advocated in structural applications to improve shear and flexural performance. In fact, when hybrid reinforcement is applied to shear-deficient members, short fibers can effectively prevent intralaminar failure by improving the ductility of the matrix [21]. Similarly, Liu et al. [22] demonstrated that the addition of high-strength fibers, i.e., steel and carbon, drastically upgraded the ductility and toughness of basalt-TRC under impact, due to the energy absorption favored by multiple crack formation and fiber extraction. As a matter of fact, fibers can effectively delay the crack initiation and, most importantly, bridge microcracks, preventing their uncontrolled propagation and thus smearing damage [23–25]. These important actions result in a significant upgrade of the toughness of the otherwise brittle mineral matrix and entail additional ductility resources in the protective structure. The synergistic contribution of textiles and short fibers can ultimately optimize the utilization of the textile [26,27] and, more remarkably, in the case of dynamic loading, the dispersed fibers strongly bolster the dissipation capacity of the composite by maintaining the bond between the textile and the matrix, thus promoting the membrane response of the TRC layer [28]. This optimal response is essential to provide the structural member with an improved self-centering attitude.

Building on the recent results showing promising improvements in the response of TRC-strengthened slabs subjected to localized impact loads [29,30], this work investigates the behavior of full-scale RC

Table 1
Test matrix summarizing the externally-bonded strengthening scenarios.

Label	Externally-bonded strengthening		
	Matrix	Fibers	Textile
B1-1-Control[a]	None	None	None
B1-2-Control	None	None	None
B2-TRC1	LC^3 concrete	None	1 layer
B3-FTRC1	LC^3-SHCC	2%vol. PE	1 layer
B4-FTRC2	LC^3-SHCC	2%vol. PE	2 layers

[a] Preliminary ping test to calibrate the shock wave series. Results are not shown.

beams strengthened with mineral-bonded protective composites and subjected to blast loads. The study is part of an international collaboration between the TUD - Dresden University of Technology, Dresden, Germany and Virginia Polytechnic Institute and State University (VT), Blacksburg, USA. The central hypothesis is that the mineral-bonded layers can improve blast performance and reduce overall component damage by: (i) promoting a broader distribution of the inelastic response, and (ii) activating the self-centering provided by the textile grids. The study focuses on the effect of strengthening layer design, including combinations of dispersed microfibers and/or continuous carbon textile grids, used to reinforce limestone calcined clay cement (LC^3) based fine-grained concrete layers. Blast loads were generated using a gaseous detonation shock tube. A single-degree-of-freedom (SDOF) analysis software, RCBlast [31], was used to simulate the dynamic deflection time histories of the tested specimens. The results are used to investigate the self-centering mechanisms, peak deflection, and residual capacity as a function of the design of the mineral-bonded composite reinforcement layer to improve existing blast protection concepts with the ultimate goal of increasing human safety, limiting resource consumption, and enhancing the diverse existing built environment.

2. Materials and methods

2.1. Test matrix and specimen design

Fig. 1 illustrates the schematic of the test setup, as well as the dimensions, internal reinforcement, and external strengthening schemes for the five beams investigated.

The test campaign was conceived to explore the blast self-centering capability of RC beams retrofitted with mineral-bonded composites consisting of a sustainable binder incorporating dispersed microfibers and/or carbon fiber textile meshes. Two of the beams, designated B1-1 and B1-2, served as replicate control specimens. The remaining three specimens were retrofitted with a 20 mm thick composite strengthening layer applied on the tensile side. The strengthening layer for beam B2-TRC1 was a textile reinforced concrete (TRC) consisting of a plain LC^3 matrix combined with a single layer of carbon textile. The strengthening for beam B3-FTRC1 was a hybrid short fiber-textile-reinforced concrete (FTRC), similar to B2-TRC1, but incorporating polypropylene (PE) microfibers fibers dosed at 2% by volume to enhance the tensile behavior of the matrix. Finally, beam B4-FTRC2 used the same SHCC matrix as B3-FTRC2 but incorporated two textile layers to investigate the effect of increasing the tensile strength of the composite. Through this selection of strengthening scenarios, summarized in Table 1, the study aimed to provide insights into the potential synergistic benefits of using fibers and textiles for enhanced blast robustness and resilience.

The simply supported beams were each 300 mm × 200 mm × 3000 mm (height × width × length). The beams were designed to be tension-controlled, exhibiting failure of the reinforcing before crushing of concrete. The tension reinforcement consisted of three ϕ10 bars ($A_s = 235.6$ mm^2, $d = 269$ mm) and two ϕ8 bars were provided in compression ($A'_s = 100.5$ mm^2, $d' = 30$ mm). Transverse reinforcement consisted of closed stirrups constructed using ϕ6 bars ($A_b = 28.3$ mm^2) spaced at 65 mm. The nominal cover depth c_v was 20 mm.
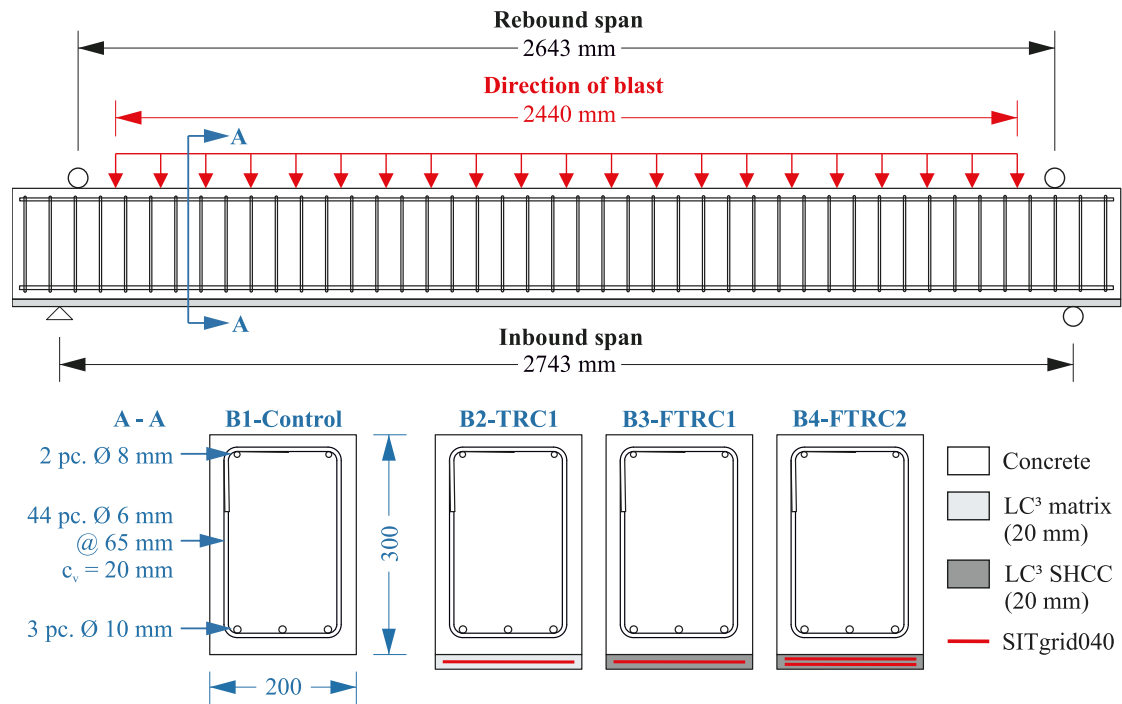
Fig. 1. Test setup and specimen designs under investigation. In the beam designations, "B" stands for beam, "F" stands for fiber reinforcement, and "TRC1" and "TRC2" for textile-reinforced concrete with a single or a double textile layer, respectively.

The RC beams were constructed with grade C35/45 ready-mix concrete using slag cement (CEM III/A 42.5N) according to the European guideline EN 206:2013+A2:2021 [32]. The specific particle size distribution of the aggregates (up to 8 mm) was chosen to ensure the concrete could penetrate the densely packed reinforcement cage. This mixture also aimed for a moderate strength development suitable for the surface treatments required in strengthening layer applications. To achieve a class F3 workability the water-to-binder (w/b) ratio was set at 0.44. The average cylinder compressive strength f_{ck} at the time of testing was 43 MPa with an average unit weight of 2200 kg/m^3. The internal steel reinforcement, comprising both longitudinal and stirrup reinforcements, utilized ribbed reinforcement steel featuring high ductility, namely B500B (characteristic yielding stress f_{yk} of 500 MPa and characteristic elongation at peak stress ϵ_{uk} of 5 %).

2.2. Strengthening layer design

2.2.1. Limestone calcined clay cement concrete

An LC^3-based fine-grained concrete was used as the matrix for the TRC and hybrid (FTRC) strengthening layers. LC^3 is a practical and effective ternary binder system, which can drastically reduce the clinker content, thereby entailing a higher degree of sustainability, and can rely on the large availability of raw sources globally [33,34]. Specifically, half of the binder (a commercially-available Portland cement, CEM I 52.5 R-SR3/NA) was replaced with a mixture of calcined clay and limestone, in a ratio of two parts clay to one part limestone. Additionally, 2.5 % of the binder content was reserved for calcium sulfate hemihydrate (CaSO$_4 \cdot \frac{1}{2}$H$_2$O), to induce proper sulfation of the binder. To tune the fresh properties of the fine concrete matrix, a poly-carboxylate-based superplasticizer and a viscosity modifying agent were added. The w/b ratio was set to 0.3, to achieve high mechanical performance [35]. The raw constituents of the mortar are given in Table 2.

2.2.2. Short fiber and textile reinforcement

Ultra-high molecular weight polyethylene (UHMWPE, abbreviated as PE) fibers with a diameter of 18 μm and a length of 6 mm were used

in beam B3-FTRC1 and B4-FTRC2. These fibers, known by their trade name as Dyneema® SK78, have a tensile strength of about 3.5 GPa, a Young's modulus of about 110 GPa, and a mean elongation at failure of 3,5 % [36]. The PE fibers are shown in Fig. 2(a).

The textile reinforcement was a semi-rigid biaxial mesh made of carbon fiber strands impregnated with polyacrylate (SITgrid040, Wilhelm Kneitz Solutions in Textile GmbH, Germany), see Fig. 2(b). This non-crimp fabric is made of 3200 tex rovings consisting of 48k filaments with a pitch of 12.7 mm along the warp direction resulting in a cross-section per unit width of 141.02 mm^2/m. In the weft direction, the rovings have a yarn count of 800 tex, consist of 12k filaments and are spaced 16 mm apart. This leads to a cross-section per unit width of 28.02 mm^2/m [37]. For both directions, Young's modulus of 205 GPa and tensile strength of 3300 MPa can be assumed as the ultimate limit state properties.

2.2.3. Strengthening application

The specimens were produced and strengthened at the Alfred-Hütter Laboratory of TUD. Immediately after placing concrete into the forms, a layer of retarder paper was placed on the fresh concrete surface of the three beams to be strengthened. After 24 h, the unhardened cement paste was removed using a high-pressure washer to make the stone aggregates (with a diameter >4 mm) of the lower side protrude from the binder and to obtain a rough surface suitable for application of the strengthening layer. The average roughness R_t was determined at the quarter points of all the beams by using the sand patch method according to Kaufmann [38], obtaining values of 0.8 mm ± 0.1 mm. The strengthening layers were applied 14 days after the concrete was cast. The surfaces of the beams were wet for 24 h prior to applying the mineral-bonded strengthening layers.

The LC^3 mortar was mixed in batches following the procedure recommended by Signorini et al. [28]. The strengthening was performed by first applying a thin layer of matrix to the moistened substrate, followed by the placing of a cut-to-size textile strip and the application of another layer of matrix. Due to the use of a single textile reinforcement in beam B2-TRC1 and B3-FTRC1, the strengthening was performed with two 1-cm layers of LC^3 concrete and fiber-reinforced matrix, respectively. For beam B4-FTRC2, which contained two textiles,

Table 2
Mix design of the LC^3 mortar, adopted as the matrix for strengthening composites.

| Raw material	Details	Dosage (kg/m^3)
Cement (CEM I 52.5 R-SR3/NA)	Holcim GmbH, Germany	610
Calcined clay	Liapor GmbH & Co.KG., Germany	387
Limestone	Saxodol®, SH minerals GmbH, Germany	194
Calcium sulfate	$CaSO_4 \cdot \frac{1}{2}H_2O$, Honeywell International Inc., Germany	31
Quartz sand	BCS413, Strobel Quarzsand GmbH, Germany	536
Superplasticizer	MasterGlenium ACE 460, MBCC Group, Germany	12
Viscosity modifying agent	UW Compound-100, Sika AG, Switzerland	2
Water	–	367

(a) PE fibers
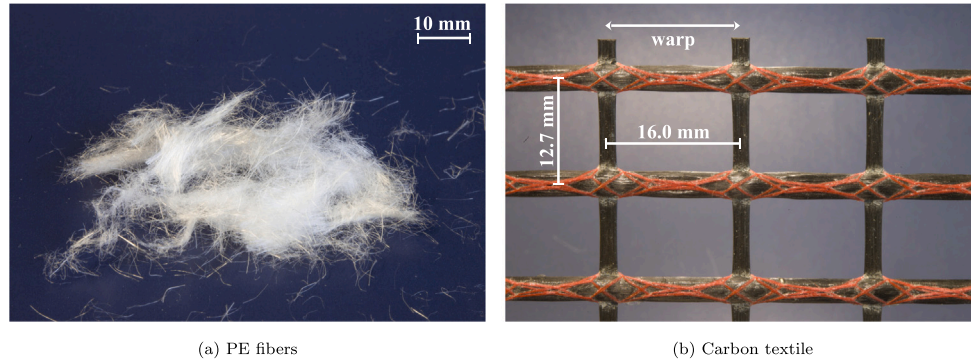
(b) Carbon textile

Fig. 2. Appearance and geometry of PE fibers and carbon textile (*Photos: Stefan Gröschel*).

three layers of fiber-reinforced matrix, with a thickness of about 6.7 mm each, were applied in series. The top surfaces were leveled and covered with wet clothing and plastic bags for the first 24 h to limit premature cracking due to water evaporation and resulting early-age shrinkage. After 28 days, all the beams were demolded.

2.3. Shock Tube Research Laboratory

Once the strengthening layers had cured sufficiently for transport, the specimens were packaged and shipped to the United States for blast testing at the VT Shock Tube Research Laboratory. The shock tube, shown in Fig. 3, is driven by an explosion of gaseous oxygen and acetylene mixtures charged into a detonation chamber. Upon ignition, the high-pressure, high-temperature shock wave generated in the detonation chamber travels down the 13 m transition section and interacts with targets mounted on the test section. The cross-sectional dimensions of the shock tube flow area at the test section are 2.44 m × 2.44 m. The pressure and impulse shock wave produced by the shock tube is controlled by the volume of detonating gases, with larger volumes of gas mixtures producing stronger blast waves. The reader is referred to Johnson et al. [5] for more information on the shock tube.

Fig. 4 shows photographs of the vertically oriented specimens mounted on the shock tube. Specimen deflections in the direction of blast wave propagation were defined as a positive (*inbound*), while deflections toward the blast source were defined as negative (*rebound*). The inbound support reaction forces were measured by load cells integral to the roller supports. As shown in Fig. 1, the free span of the inbound simple supports was 2743 mm. To prevent the specimen from falling back into the shock tube during rebound deflections, a rebound support with a clear span of 2643 mm was provided. The beams were subjected to a centrally applied, partially distributed, uniform blast load over 2440 mm.

A load transfer device (LTD) was used to collect and transmit the blast pressure generated by the shock tube to the test specimen through a series of concentrated point loads [4]. LTDs are necessary when testing non-planar members in a shock tube that require full reflection of the blast wave [14,16,39]. The LTD consisted of a 2.13 m × 2.44 m aluminum sheet stiffened by 11 evenly spaced aluminum beams. To ensure that the LTD remained in contact with the beams during testing, the entire assembly was loosely clamped to the test specimen. The area of the LTD, A_{LTD}, and mass, m_{LTD}, were 5.2 m^2 and 225 kg, respectively.

The applied pressure time histories were recorded by two pressure transducers (PT1 and PT2) mounted on the shock tube walls 50 mm away from the reflecting surface of the LTD on each side of the specimen. The simple supports at the top and bottom of the beam were equipped with load cells (LC) to measure the inbound reaction forces. Redundant measurements of the mid-span deflections of the specimens were obtained using both a linear potentiometer (LP) and a non-contact laser deflection transducer (LS1). Another laser deflection transducer (LS2) captured the motion of the shock tube reaction frame to which the specimens were mounted. Test data was recorded at 800 kHz. To visually document the specimens' responses to the blast loads, two high-speed cameras were used: one capturing a side profile view perpendicular to the shock tube's motion, and the other providing a comprehensive isometric view of the tests. All beams were subjected to the same series of four blasts of increasing intensity. Following the protocol proposed by Johnson et al. [5], the first blast was aimed at activating the elastic behavior of the specimen, two intermediate blasts were aimed at the yield strength and the inelastic reaction of the beams, and eventually a fourth blast was targeted close to the ultimate capacity of the specimen. The first beam (B1-1-Control) served as a pilot specimen to determine the appropriate volumes of oxygen-acetylene to achieve the objectives described. The pilot beam was loaded by a sequence of four shots with volumes of 0.028 m^3 (1 ft^3), 0.085 m^3 (3 ft^3), 0.198 m^3 (7 ft^3), and 0.311 m^3 (11 ft^3). The last two shots were too powerful and a refined four shot pattern of 0.028 m^3 (1 ft^3), 0.085 m^3 (3 ft^3), 0.142 m^3 (5 ft^3), 0.198 m^3 (7 ft^3) was determined to be optimal for comparing the blast capacity of the remaining beams B1-2-Control, B2-TRC1, B3-FTRC1, and B4-FTRC2.
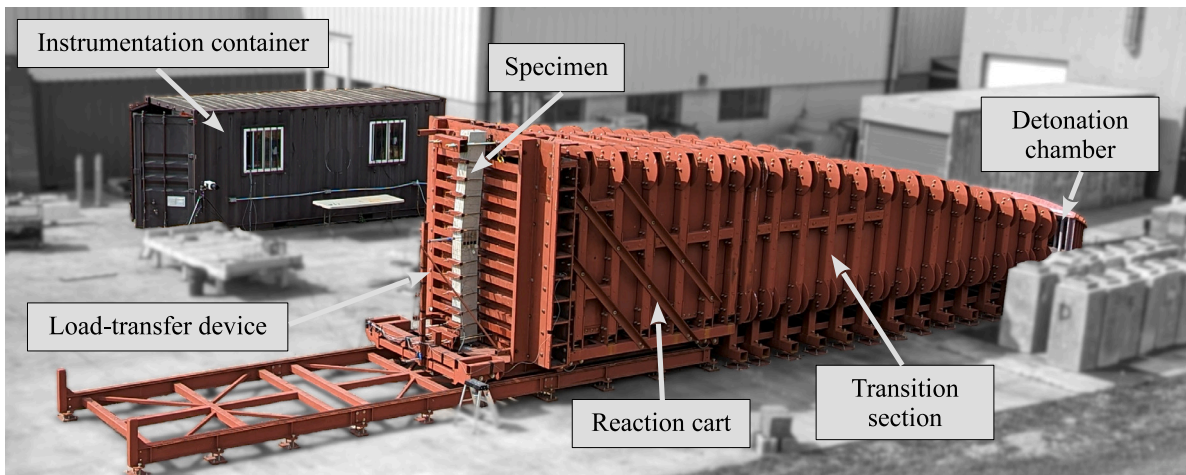
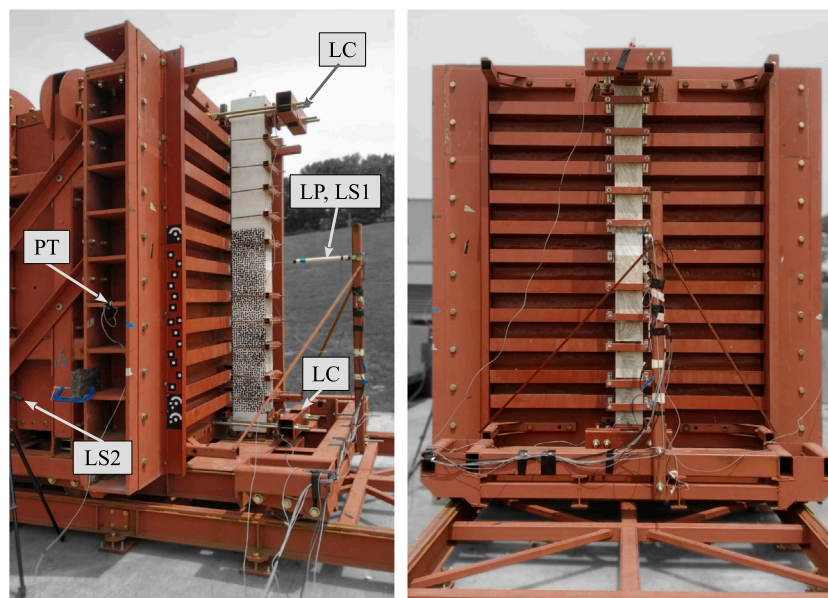**Fig. 3.** Photograph of a test specimen mounted to the shock tube.

Fig. 4. Specimen, support conditions, and instrumentation at the test section of the Virginia Tech Shock Tube.

3. Results and discussion

3.1. Statistical evaluation of the blast protocol

Fig. 5 shows a comparison of the typical reflected pressure time (P_r) histories of the four progressively increasing blast tests conducted in this study. For clarity, the four blast tests are offset graphically by 20 ms.

The primary shock is the largest, followed approximately 60 ms later by the secondary shock, which occurs after the primary shock has traveled down the length of the shock tube and back to the LTD. The secondary shock was due to internal reflections of the shock within the shock tube due to incomplete venting. The tertiary shock follows another 60 ms later. The pressure signature of the tertiary shock has effectively dissipated and is ignored. The shock tube demonstrated excellent repeatability in generating blast waves, as evidenced by a coefficient of variation (CoV) of approximately 6% for the average peak pressure and impulse of the primary wave in Blasts 2, 3, and 4. However, the initial 'ping test' (Blast 1) exhibited the greatest variability, with a CoV exceeding 50%, primarily due to the challenges associated with handling such a small volume of gas.

3.2. Key mechanical parameters and deflection time histories

Fig. 6 presents a comparison of the beam mid-span deflection time histories for each of the four blast tests performed. Key parameters of the experimental results are presented in the Appendix (see Table A.3), where the shock wave parameters are summarized in terms of the maximum reflected pressure (P_r) and reflected impulse (I_r) of the primary and secondary pressure waves, as well as the arrival time (t_a) of a substantially attenuated secondary shock relative to the arrival of the primary shock.

In addition, maximum deflection d_{m1} and time to maximum deflection t_{m1} due to the primary shock, the maximum deflection d_{m2} and time-to-maximum deflection t_{m2} due to the secondary shock, and the final residual deflection, d_r are also reported and discussed in the following sections. The maximum support rotation $\theta_m = \arctan\left(2d_{max}/L_n\right)$ was also computed. All deflections reported in this paper are relative to the original position of the specimen prior to testing.

As a key performance indicator of the efficiency of the strengthening layers, the Blast Self-Centering Index (BSI) was calculated for each blast event i. The original definition of BSI, based on the approach of Johnson et al. [5], was adapted in the present study, and now takes
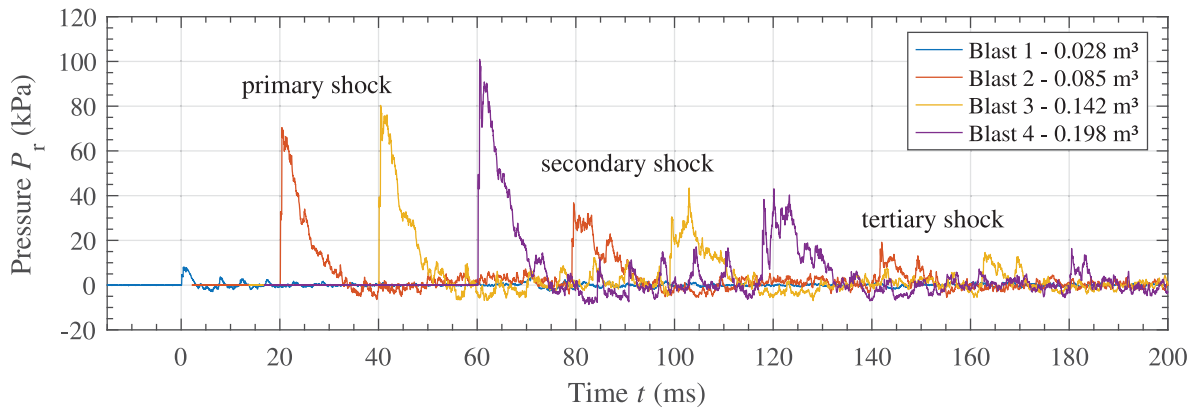
Fig. 5. Pressure–time–history of blast protocol on experiment B1-2-Control (with 20 ms offset). (For interpretation of the references to color in this figure legend, the reader is referred to the web version of this article.)
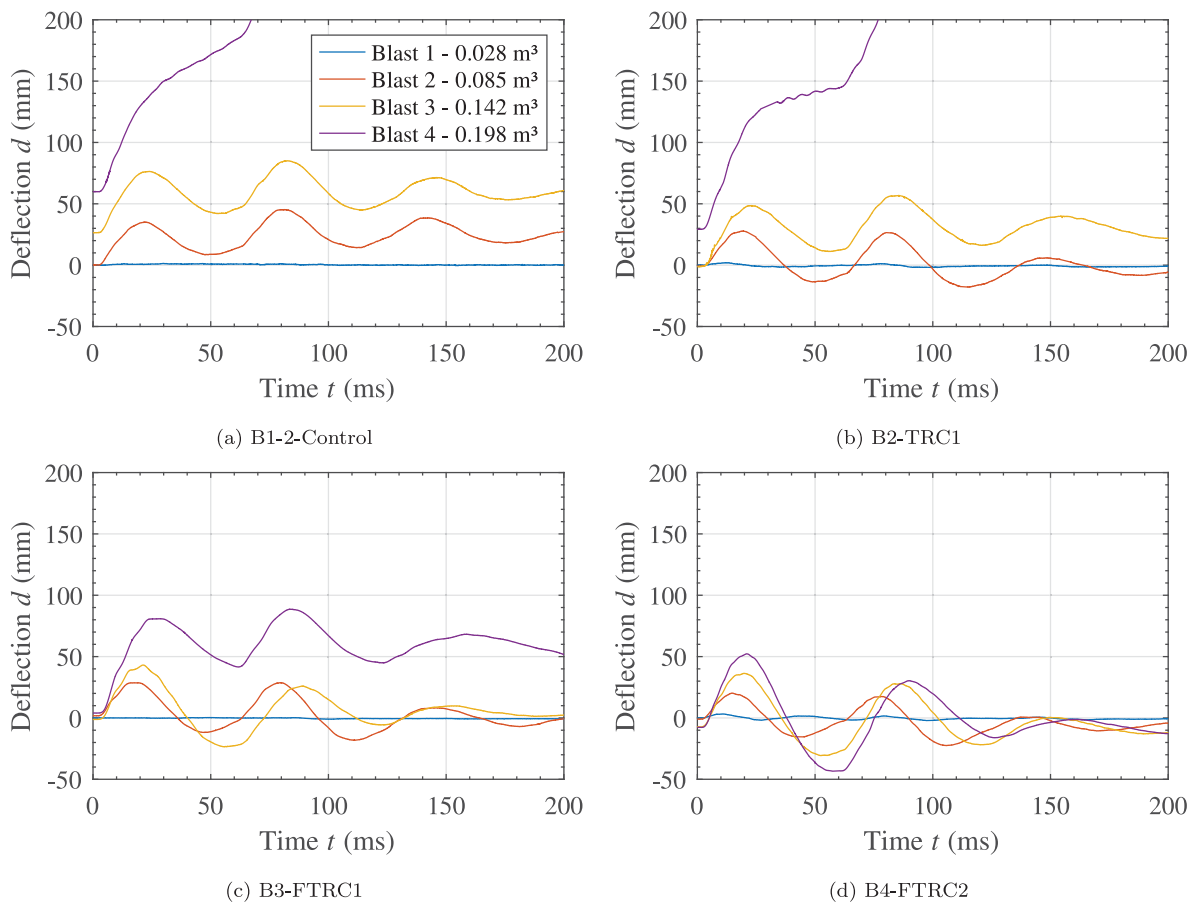

(a) B1-2-Control

(b) B2-TRC1

(c) B3-FTRC1

(d) B4-FTRC2

Fig. 6. Comparison of experimentally recorded midspan deflection time histories. (For interpretation of the references to color in this figure legend, the reader is referred to the web version of this article.)

into account the ratio of the net residual displacement and the actual deflection caused by each individual blast event, as shown in Eq. (1):

$$BSI_i = 1 - \frac{d_{r,i} - d_{r,i-1}}{d_{m,i} - d_{r,i-1}} \quad (1)$$

The BSI provides a relative measure of the extent to which the maximum deflection is recovered in each individual test. In the best-case scenario, full self-centering is achieved when the beam is able to recover the total deflection induced by the blast without any residual deflection ($BSI = 1$). On the contrary, no self-centering behavior corresponds to the case where the maximum deflection induced by

the blast load is the permanent deformation ($BSI = 0$). A BSI value greater than 1 is also possible if the component has a negative residual deflection compared with the previous residual.

3.3. Evaluation of the beam response

3.3.1. Blast 1
The first shot in the sequence was intended to inspect the elastic response of the beams. No significant damage was observed in any of the specimens after this shot. After Blast 1, B1-2-Control exhibited no visible cracks and experienced a maximum deflection of 1.6 mm with no

(a) B2-TRC1

(b) B3-FTRC1

Fig. 7. Appearance of the mid-span after Blast 3 showing the influence of the addition of short fibers regarding the crack pattern and spalling retainment.

residual deflection, thereby demonstrating the elastic response ($BSI \sim$ 1). Prior to testing B2-TRC1, fine shrinkage cracks were observed in the LC^3 matrix layer and no new cracks formed afterwards. As expected, this was also observed for specimens B3-FTRC1 and B4-FTRC2.

3.3.2. Blast 2

As a result of Blast 2, B1-2-Control developed flexural cracks along the central hinge area up to two-thirds of the clear span. The maximum deflection was 47.4 mm with a corresponding residual deflection of 26.5 mm and a BSI of 0.44, due to the yielding of the internal steel reinforcement. B2-TRC1 exhibited predominantly elastic behavior, with a maximum deflection of 27.7 mm and a residual deflection of −1.7 mm. Numerous parallel cracks developed across the width of the strengthening layer, while only a few flexural cracks were visible on the sides of the beam. B3-FTRC1 underwent a maximum inbound deflection of 28.7 mm and a maximum rebound deflection of −18.4 mm, followed by a residual deflection of −1.2 mm. In addition, flexural cracks extending to approximately two-thirds of the height of the beam were observed, along with a dense pattern of interconnected horizontal cracks in the FTRC layer. B4-FTRC2 had a maximum inbound deflection of 17.5 mm and a maximum rebound deflection of −22.4 mm. The residual rebound deflection recorded for this specimen was attributed to rebound deflections exceeding the yield capacity of the member during moment reversals. The significant moment reversal on the less reinforced, nominal compression side, resulted in increasingly negative residual deflections from −0.3 mm to −7.3 mm.

3.3.3. Blast 3

The trend of increasing deflections for B1-2-Control continued in Blast 3, with maximum and residual deflections of 85.0 mm and 59.9 mm, respectively, denoting of a fully inelastic response. At this point, B1-2-Control had significant observable deformation and a handful of wide cracks around the mid-span. The damage in each beam after Blast 3 can be seen in Fig. 7. Blast 3 caused significant maximum (56.9 mm) and residual (29.3 mm) deflections for B2-TRC1, resulting in a BSI of 0.47. This was accompanied by a partial failure of the cementitious overlay, with 1.95 kg of TRC spalling off over a central area of 45 cm, exposing the textile grid (see Fig. 7(a)). It should be noted that the spalling mass and area of the TRC layer for B2-TRC1 is underestimated due to the connections between the LTD and the test specimen. Conversely, this is not the case for B3-TRC1 with dispersed fibers, where no spalling was observed (see Fig. 7(b)). Despite the scattering of debris within a radius of 2.5 m, the overall crack pattern in the strengthening layer remained unchanged, indicating that the textile grid was still intact, although permanent strains occurred in the tensile steel reinforcement. B3-FTRC1 exhibited increased oscillatory inbound and rebound deflections, with an inbound residual deflection of 4.0 mm, indicating yielding of the tensile reinforcement. B4-FTRC2 incurred additional damage to the compressive reinforcement and yielding of the tensile reinforcement, as the specimen's residual displacement shifted only slightly from −7.3 mm to −7.7 mm.
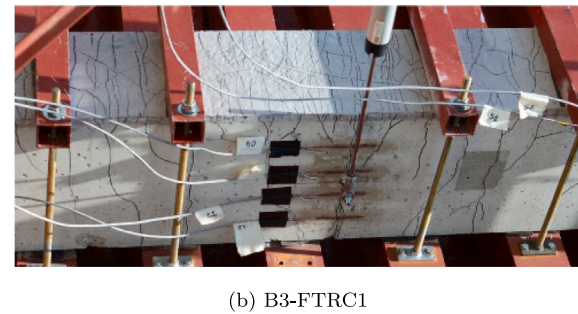
At this point, B3-FTRC1 and B4-FTRC2 had developed many cracks, however, compared to B1-2-Control and B2-TRC1 the cracks were narrower, there was neither significant spalling nor obvious observable residual deformation.

3.3.4. Blast 4

During Blast 4, the tensile steel reinforcement of B1-2-Control fractured at mid-span, resulting in the complete splitting of the beam from the secondary shock load. For B2-TRC1, the blast caused both the textile and steel reinforcements to fracture at mid-span, culminating in complete failure and splitting of the specimen. This failure, triggered by the secondary shock load, mirrored the behavior observed in the B1-2-Control. After the final blast, the strengthening layer of the B3-FTRC1 displayed an extensive network of cracks, but did not eject hazardous debris, unlike B2-TRC1. However, the significant maximum and residual deflections of 88.7 mm and 59.3 mm, respectively, along with a prominent central crack in the retrofit and noticeable damage to the textile, indicated that the beam was nearing failure with minimal residual capacity. B4-FTRC2 experienced a maximum inbound deflection of 52.3 mm, a maximum rebound deflection of −43.5 mm, and a residual deflection of −7.1 mm.

During the final test, one major crack formed on the sides of the beam and crushing of the concrete cover on the inbound compression side was observed. However, it is important to note that B4-FTRC2 did not undergo global failure or spalling. The mineral-bonded strengthening layer retained its structural integrity, indicating that the specimen likely had considerable residual capacity after the final blast. Photographs of the beams after Blast 4 are shown in Fig. 8. A comparison of the extent and progression of damage in the beams during Blast 4 can be seen in the multimedia video file, available in the online version of this paper.

3.4. Deflection and blast self-centering tendency

Fig. 9 presents bar graphs showing the maximum (a) and residual (b) deflections observed across all tests, which were conducted at increasing blast intensities and are represented by different colors. Additionally, the percentage variation between different beam configurations is displayed for each blast intensity, with the exception of the ping tests (Blast 1). In addition, Fig. 9(c) shows the BSI trend (see Eq. (1)) as a function of the dimensionless ductility ratio μ. The ductility ratio is defined as the ratio of the maximum beam deflection (d_m) to a reference deflection value d_{yield} at which the internal rebar of the control beam yields ($d_{yield} = 8$ mm). As a consequence, in Fig. 9(c), data points at $\mu < 1$ reflect the beam response in the elastic regime. In the following subsections, the specific influence of the addition of fibers and textiles in the reinforcement layer is examined separately based on the values here presented.

(a) B1-2 (control)   (b) B2-TRC1   (c) B3-FTRC1   (d) B4-FTRC2

Fig. 8. Photographs depicting the progression of damage in beams after Blast 4.

3.4.1. Effect of dispersed PE microfibers

In order to pinpoint and quantify the role of short PE fibers on the blast response of the mineral-bonded strengthening layers, spotlight is set on the specimens B2-TRC1 (single-ply textile grid embedded in plain fine-grained mortar) and B3-FTRC1 (single-ply textile grid embedded in a fiber-reinforced matrix). The addition of fibers led to a reduction in the maximum deflection and the residual deflection of 4 % and 29 %, respectively, for Blast 2. This effect was even more pronounced with increasing blast energy input, namely 24 % and 86 %, respectively, for Blast 3. Due to the very low residual deflections recorded for Blast 2, only a modest difference in the BSI values could be detected at this stage, as the textile alone can effectively act as a self-centering element and both beams could almost recover the pristine shape. However, as the external load increases and with it the maximum deflection, a drop in the BSI could be observed for B2-TRC1 up to approximately 47 %, denoting a lower efficiency of the textile reinforcement. On the contrary, the BSI for the B3-FTRC1 counterpart showed only a slight decrement from the optimal threshold of 100 % (for Blast 3 it was 88 %). In general, these tests prove that the use of fibers leads to some improvement in the self-centering attitude of the retrofitted beams. However, the main role is played by the textile once its effectiveness is secured by a certain extent of ductility of the embedding medium, as discussed in the following section. At the same time, the use of PE fibers has a positive effect on the damage pattern, with the already described drastic reduction of spalling (see Fig. 7) and the increase of the maximum load-bearing capacity (see Fig. 8). This gain in performance of hybrid strengthening solutions is mainly due to the formation of a large number of fine cracks and to the crack-bridging ability of the fibers in the LC^3-SHCC used. These improved damage pattern ultimately results in a greater activation of the inner textile strengthening layer. In effect, the textile is prevented from sudden and premature delamination due to matrix fragmentation, thereby resulting in increased energy absorption

and better protection of the retrofitted RC beam. Similar results of improved post-crack tensile strength, increased ductility and damage tolerance, as well as elimination of secondary fragments were also described by Burrell et al. [40] and Aoude et al. [41] who performed similar shock tube tests on steel fiber reinforced concrete (SFRC) and ultra-high performance fiber reinforced concrete (UHPFRC) columns with steel fiber contents ranging from 0.5 % to 6.0 %. While these results were obtained with structures composed entirely of steel fiber RC, the effect in the present work was achieved by the addition of only a thin mineral-bonded layer, extending the observations of Signorini et al. [28] to thin fiber-reinforced members.

3.4.2. Effect of the number of textile reinforcement plies

Specific considerations concerning the influence of increasing number of textile plies on the blast response of retrofitted RC beams were obtained by comparing the specimens with hybrid fibrous reinforcement, namely B3-FTRC1 with one textile grid and B4-FTRC2 with two textile grids embedded in the LC^3-SHCC matrix. The addition of an extra textile layer was found to mitigate the peak deflections for Blasts 2, 3, and 4 by 39 %, 16 %, and 41 %, respectively. Most remarkably, doubling the continuous carbon reinforcement resulted in a distinct and consistent switch in the failure mode of the beam, as clearly indicated by the negative residual deflections for B4-FTRC2. This behavior is explained by the yielding of the steel rebar in the compressed zone, which was reached upon rebound. In fact, in the case of B4-FTRC2, there is a significant gap between the total reinforcement ratio in the tensile and compressive zones, the latter being too weak to withstand the rebound (negative) moment and thus to self-center. In any case, the combined use of two plies of textile and dispersed PE fibers preserves the BSI close to unity, even with very pronounced external shock waves and in the presence of high deflections, where other beams either failed completely or resulted in significant irreversible deflections. In
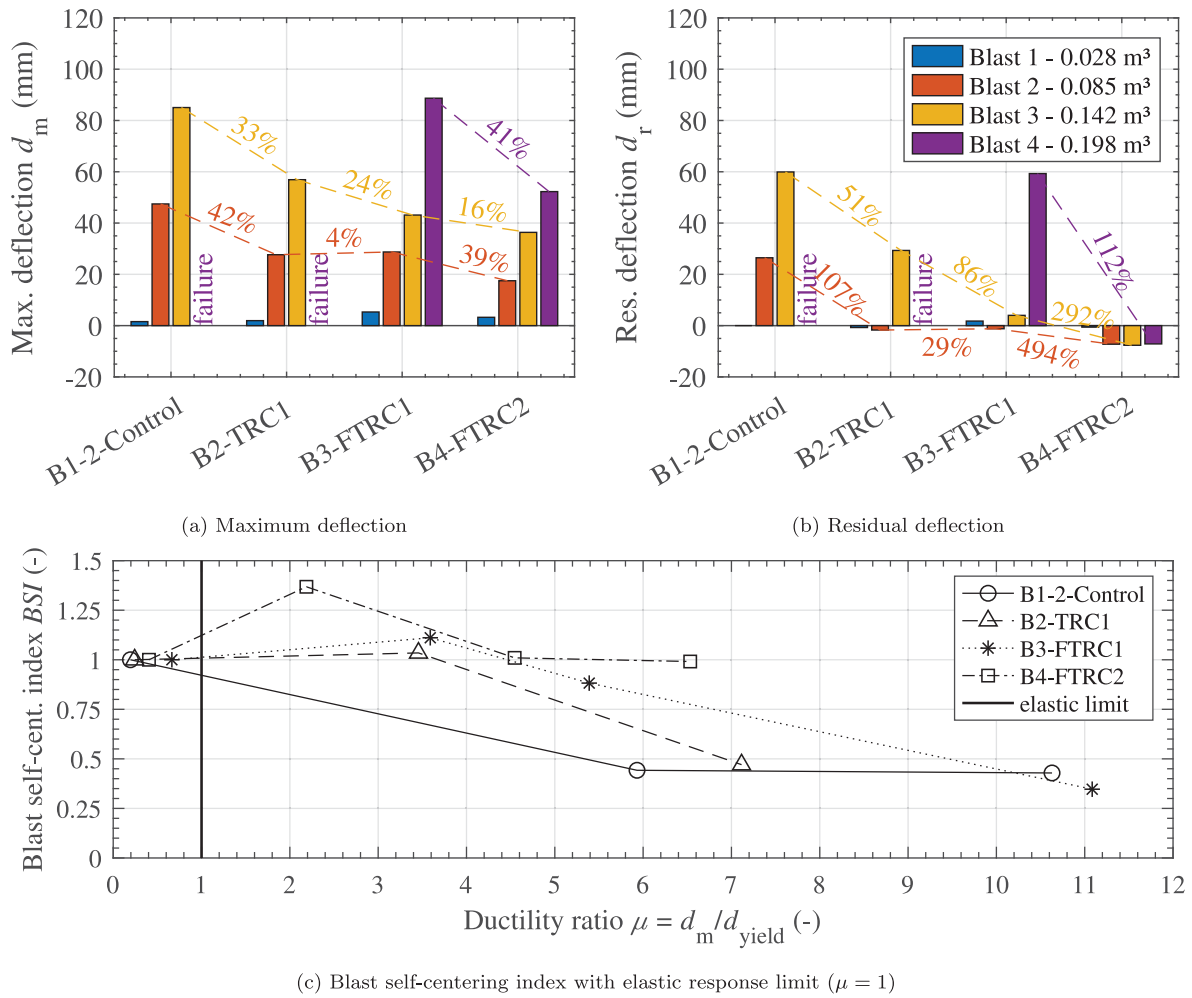
(a) Maximum deflection

(b) Residual deflection

(c) Blast self-centering index with elastic response limit ($\mu = 1$)

Fig. 9. Comparison of the specimens based on relevant performance indicators. (For interpretation of the references to color in this figure legend, the reader is referred to the web version of this article.)

addition to the remarkable damage reduction and energy dissipation capability provided by the short fibers, an adequate number of textile layers is primarily governing the self-centering behavior of the composite structure. This result mirrors the trends observed in the studies of Crawford [42] who investigated full-scale fiber reinforced polymer (FRP) wrapped RC columns using in-field blasts, as well as Jacques [43], Jackson et al. [16] and Johnson et al. [4], who investigated FRP retrofitted RC members and hybrid RC beams in shock tube tests. In addition to such epoxy-based systems, the present work shows that mineral-bonded retrofits also hold promise for significantly improving the blast resistance and resilience of structures while mitigating thermal stability concerns.

4. Single-degree-of-freedom dynamic analysis

Single Degree of Freedom (SDOF) analytical models, known for their effectiveness in simulating the blast performance of structures, were used to predict the response of blast-loaded specimens. The objective was to develop tools to capture the role of the mineral-bonded composites on the overall load–deflection behavior of the retrofitted beams. The analysis also examined the hysteretic response of the beams to understand how the strengthening layers contributed to mitigating residual damage in beams that would otherwise have failed catastrophically without the strengthening layers.

4.1. Analysis approach

Fig. 10 shows the dynamic stress–strain relations used in the analysis. These were generated by applying a dynamic increase factor (DIF) to the quasi-static stress–strain relations to account for strain rate effects. A strain rate of $0.01\,\mathrm{s}^{-1}$ was conventionally assumed for all analyses. This rate falls within the range observed during the shock tube tests, which varied from about $0.01\,\mathrm{s}^{-1}$ for the first two tests to $1.0\,\mathrm{s}^{-1}$ for the most severe tests.

The model of Kent and Park [44] was used for the unconfined cover concrete shown in Fig. 10(a), with a concrete cylinder strength of $f_\mathrm{c}' = 43$ MPa obtained from standard cylinder tests. A DIF of 1.15 was applied to the unconfined concrete based on the CEB-FIB Model Code 2010 [45] for the dynamic compressive strength of concrete. For the concrete constrained by the transverse reinforcement, as shown in Fig. 10(b), the confined concrete model of Scott et al. [46] was used with a DIF of 1.14. [45]. The tensile stress–strain response of the SHCC of B3-FTRC1 and B4-FTRC2 shown in Fig. 10(d) was obtained from tensile dumb-bell coupon tests [28]. Owing to uncertainties in the dynamic stress–strain behavior of the material and the absence of sufficient data in the literature, no DIF was applied to the SHCC tensile stress–strain data used in the analysis. For the dynamic tensile stress–strain relationship of the longitudinal steel reinforcement displayed in Fig. 10(c), a DIF of 1.11 and 1.03, respectively, was applied to the yield and ultimate strengths obtained from the coupon test data [47]. The model of Yalcin and Saatcioglu [48] was used to consider the possible instability of the

(a) Unconfined concrete [44]

(b) Confined concrete [45]

(c) B500B Steel [46]

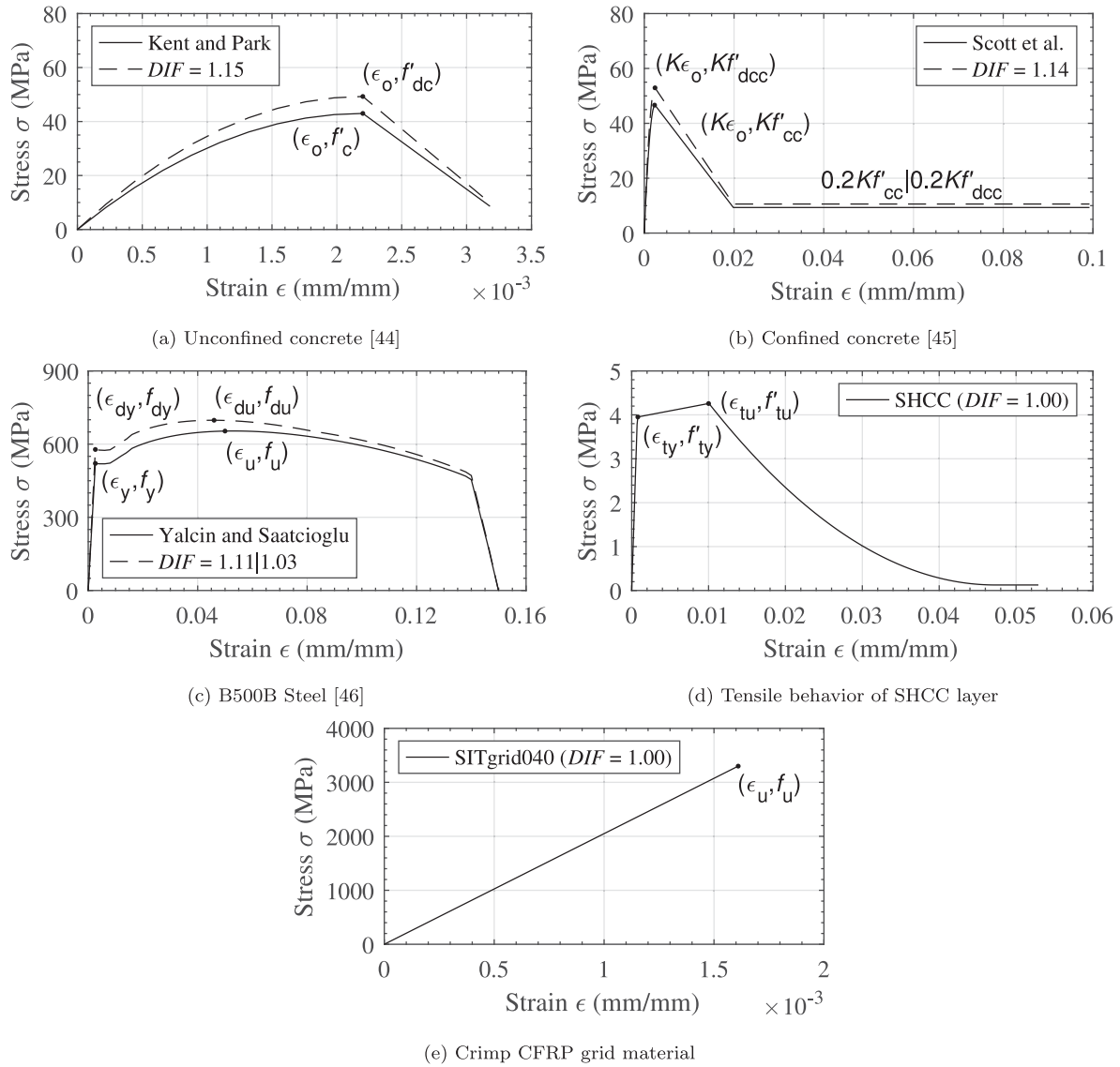(d) Tensile behavior of SHCC layer

(e) Crimp CFRP grid material

Fig. 10. Stress–strain models used in dynamic SDOF modeling.

compression reinforcement in bending. This model predicted that the compression bars would begin unloading after yielding but before the onset of strain hardening, as illustrated in Fig. 10(c). A linear elastic stress–strain relationship was assumed for the tensile response of the carbon textile layers based on the manufacturer's data, as shown in Fig. 10(e). Based on the recommendation of Jacques et al. [14], no *DIF* was applied to the textiles, as uniaxially acting carbon fabrics appear to be insensitive to strain rate. A perfect bond between the matrix and the reinforcing textile is assumed for the modeling.

The development of the resistance function began with the generation of moment–curvature relationships for each of the cross-sections shown in Fig. 1. Positive bending of the cross section was used to develop the inbound resistance, while negative bending was used to develop the rebound resistance. The global deformations of the beams subjected to a partially uniformly distributed load were determined by numerical integration of the curvature distribution along the beam length at incremental loading stages. The analysis of the inbound and rebound resistance functions for each specimen was performed by first discretizing the member into 100 elements along its clean bending span. For each load increment, the curvature distribution along the span was determined using moment–curvature relationships. Integration of the curvature distribution was performed to determine the deflected shapes, which in turn were used to compute equivalent SDOF load-mass transformation factors [49]. The solution algorithm proposed by Jacques [43] was used to identify the post-peak unloading branches of the resistance functions.

A comparison of the analytical resistance functions for each of the four beams is presented in Fig. 11. Each of the three strengthened beams exhibited a significant enhancement in strength compared to the unstrengthened control specimen. With each increment in the external strengthening (from B2 to B4), there was an increase in both the peak resistance and energy absorption. B4-FTRC2, reinforced with two textile grids, was the strongest beam, while the addition of PE microfibers in B3-FTRC1 yielded moderate increases in strength and stiffness over the plain fine LC^3 concrete matrix B2-TRC1. All of the strengthened beams experienced a sudden loss of resistance after rupture of the textile grids, and generally matched the resistance characteristics of the control beam thereafter. The influence of the mineral-bonded strengthening layer on the rebound resistance was assumed to be negligible, and as a result, all beams were assumed to have the same rebound resistance function as B1-Control.
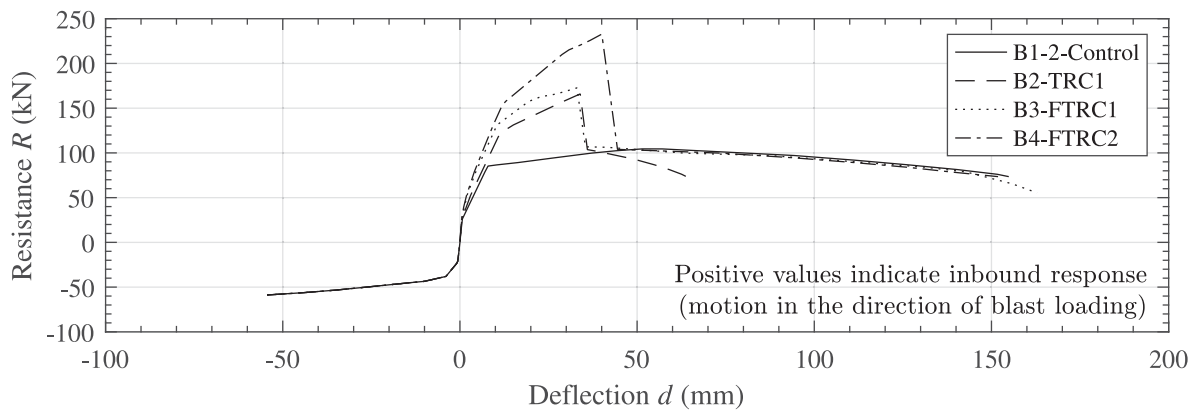
Fig. 11. Comparison of the resistance functions used in the SDOF analyses.

4.2. SDOF analysis

The analysis was performed by solving the SDOF equation of motion, given in Eq. (2):

$$k_{LM}[u(t)]\, m\ddot{u}(t) + c\dot{u}(t) + R[u(t)] = AP_r(t) \tag{2}$$

where $u(t)$, $\dot{u}(t)$ and $\ddot{u}(t)$ are the displacement, velocity, and acceleration of the active degree of freedom at midspan, respectively; $k_{LM}[u(t)]$ and $R[u(t)]$ are the load-mass transformation factor and resistance function, respectively; $A = 5.1\,\mathrm{m}^2$ is the area of the LTD impacted by the blast wave, m is the total mass of the system including the specimen and the LTD (taken as $601\,\mathrm{kg}$ for B1 and $630\,\mathrm{kg}$ for B2, B3, and B4), c is a damping coefficient (taken as 5% of the critical damping ratio, $c_c = 2\sqrt{k\,m\,k_{LM}}$), and $P_r(t)$ is the applied blast pressure time–history recorded during the shock tube tests.

All analyses were conducted with a time step Δt of $0.01\,\mathrm{ms}$, which yielded satisfactory results. The simulations were terminated either when the deflection reached a steady state or when it surpassed the maximum deflection outlined in the resistance function, indicating a blowout failure. The equation of motion, shown in Eq. (2), was numerically integrated using RCBlast [31]. This software tool relies on a predictor–corrector scheme solution algorithm, essential for handling the nonlinear resistance and load-mass transformation functions.

An accumulated damage hysteretic (ADM) model was used to account for the effects of repeated blast testing on the strength and stiffness of the test specimens [14]. This hysteretic model uses deflection data predicted from previous tests as seed data to analyze subsequent tests. The ADM establishes the initial reloading curve in the SDOF system as the line connecting the residual deflection in the previous test to the point on the resistance function corresponding to the maximum inbound deflection from that test. The ADM then tracks along the backbone resistance function until a local maxima and unloads according to an unloading stiffness, k_u. The value of k_u was adjusted based on the type of strengthening and the number of blast tests conducted. Initially, the unloading stiffness was assumed to match the elastic stiffness of the members. For subsequent loading, it was reduced as necessary to ensure the displacement time-histories aligned closely with the experimental results. The next section will discuss the empirically calibrated values of unloading stiffness, the corresponding predictions, and how they vary across different strengthening approaches. The model also includes specific rules for the transition between rebound and inbound responses. A detailed description of the ADM can be found in the paper by Johnson et al. [4]. In addition, a preliminary SDOF analysis was performed to verify the contribution to blast resistance provided by the additional mass of the mere thickening of the beam cross section induced by the externally-bonded strengthening. The analysis highlighted that the increase of mass of the beam itself ($29\,\mathrm{kg}$, i.e. 5% of the total beam mass), i.e. the specific density, despite

an expected slight reduction of the peak displacements (in any case lower than 12%), could not affect the predicted failure, which remains the same as the control beam B1-Control.

4.3. Comparison of analytical and experimental results

Fig. 12 displays a comparison of selected experimental and analytical results, namely Beam B2-TRC1 Blast 2 (Fig. 12(a)), Beam B3-FTRC1 Blast 3 (Fig. 12(b)), and Beam B4-FTRC2 Blast 4 (Fig. 12(c)). For each test shown, the left column shows the experimentally recorded reaction forces superimposed on the predicted resistance function and hysteretic loop. The right column shows a comparison of the experimental and predicted time histories of the mid-span deflection. Fig. 13a–b presents a comparison between the experimental and predicted results for the response of all RC beams under blast loading.

The results show a strong correlation between the predicted and experimental deflection of the beams under the primary and secondary shock, with the majority of the points clustering around the lines of unity, indicating accurate predictions. Furthermore, the proposed methodology was able to reasonably capture the deflection recovery and residual deflection of the beams, as can be seen from the deflection time histories shown in Fig. 12 and the *BSI* comparisons shown in Fig. 13(c). Therefore, the good agreement of the predictions at the peak displacement response can be attributed, at least in part, to the use of resistance functions and transformation factors that capture the gradual formation of inelastic response in all cross-sections, as well as a hysteretic model capable of capturing the general effect of accumulated damage and self-centering of retrofitted beams. However, an empirical calibration of the unloading stiffness K_u was required for certain specimens to account for the stiffness degradation due to progressively increasing repeated blast tests.

Fig. 13(d) illustrates the empirically determined unloading stiffness K_u, normalized with respect to the elastic stiffness K_e for each beam, plotted against the ductility ratio μ. The ductility ratio was defined as the maximum predicted deflection divided by the yield deflection of the member. The results of the analysis indicated that the control beams, B1-1 and B1-2, exhibited no significant stiffness degradation from repeated testing up to a ductility ratio $\mu = 10$. In the case of beams B3-FTRC1 and B4-FTRC2, which incorporated PE microfibers, setting K_u equal to K_e yielded satisfactory results up to a $\mu = 2$. For tests producing higher ductility ratios, accurate SDOF predictions were achieved only when the unloading stiffness K_u was assumed to be less than K_e. Similar reductions in K_u were not observed for B2-TRC1, which was attributed to the fact that the SDOF results for the third blast test did not agree well with the test data, irrespective of the value of K_u. This may be due to spalling of the matrix, which could have compromised the full-bond assumption for the textile layer during Blast 3. The plateau in unloading stiffness K_u observed for
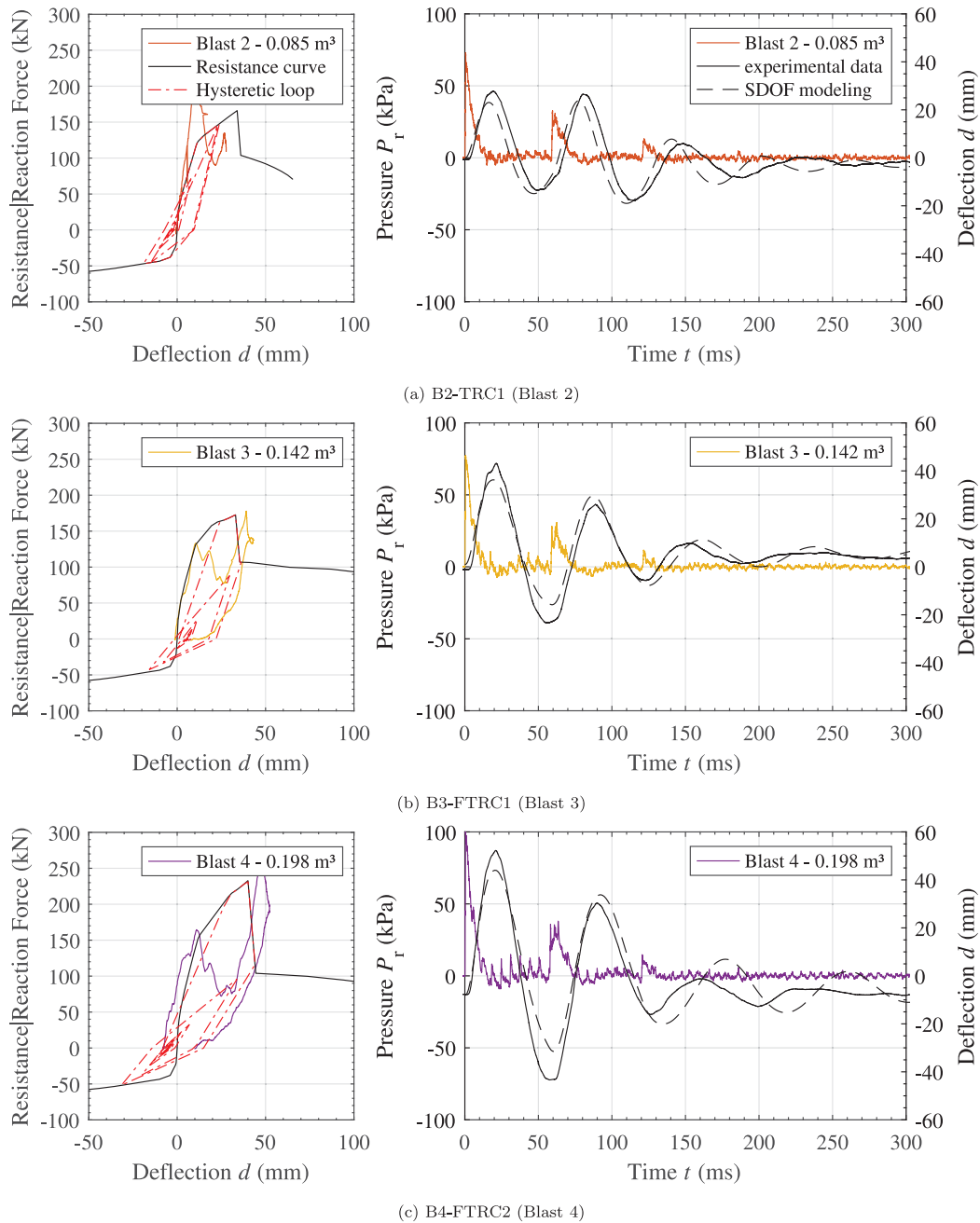
Fig. 12. Hysteretic response and displacement time history comparison of experimental and predicted. (For interpretation of the references to color in this figure legend, the reader is referred to the web version of this article.)

B3-FTRC1 within the ductility ratio range of μ = 3.5 to 7.5 was attributed to the loss of restoring force provided by the textile grid that fractured during the penultimate blast. Nevertheless, the analysis indicated that the global softening of the unloading stiffness for B3-FTRC1 and B4-FTRC2 allowed these beams to recover a greater portion of their maximum deflections compared to the control beams. This improvement resulted in lower residual deflections and, consequently, lower overall damage levels. This beneficial self-centering behavior is attributed to the synergistic effect of the restoring force produced by the textile grids and the crack-bridging energy absorption of the PE fibers in the SHCC matrix.

Fig. 14 compares the analytical resistance functions, including the unloading stiffness K_u used in the ADM algorithm, with the inbound support reactions for all four blast tests on beams B1-2 Control and B4-FTRC2. The analytical resistance functions generally provide accurate estimates of the strength and stiffness evolution derived from the in-bound support reactions. For the conventionally reinforced B1-2 beam, the unloading slopes show minimal stiffness degradation with increasing blast pressures, with values of K_u approximately equal to the initial elastic stiffness K_e throughout the response. Conversely, the mineral-bonded specimen B4-FTRC2 shows evidence of a progressive unloading stiffness degradation with increasing blast magnitude, providing a self-centering effect which contributed to the reduction in residual damage levels. The notable sharp spikes in the reaction force data, particularly evident in beam B1-2 shown in Fig. 14(a), and also present in the reaction load cell data shown in Fig. 12, warrant acknowledgment. These spikes are thought to result from higher order effects due to the dynamic interaction between the beam, the attached LTD, and the reaction cart on which the specimens are mounted. In certain cases, these high-order effects are known to generate inertial forces that
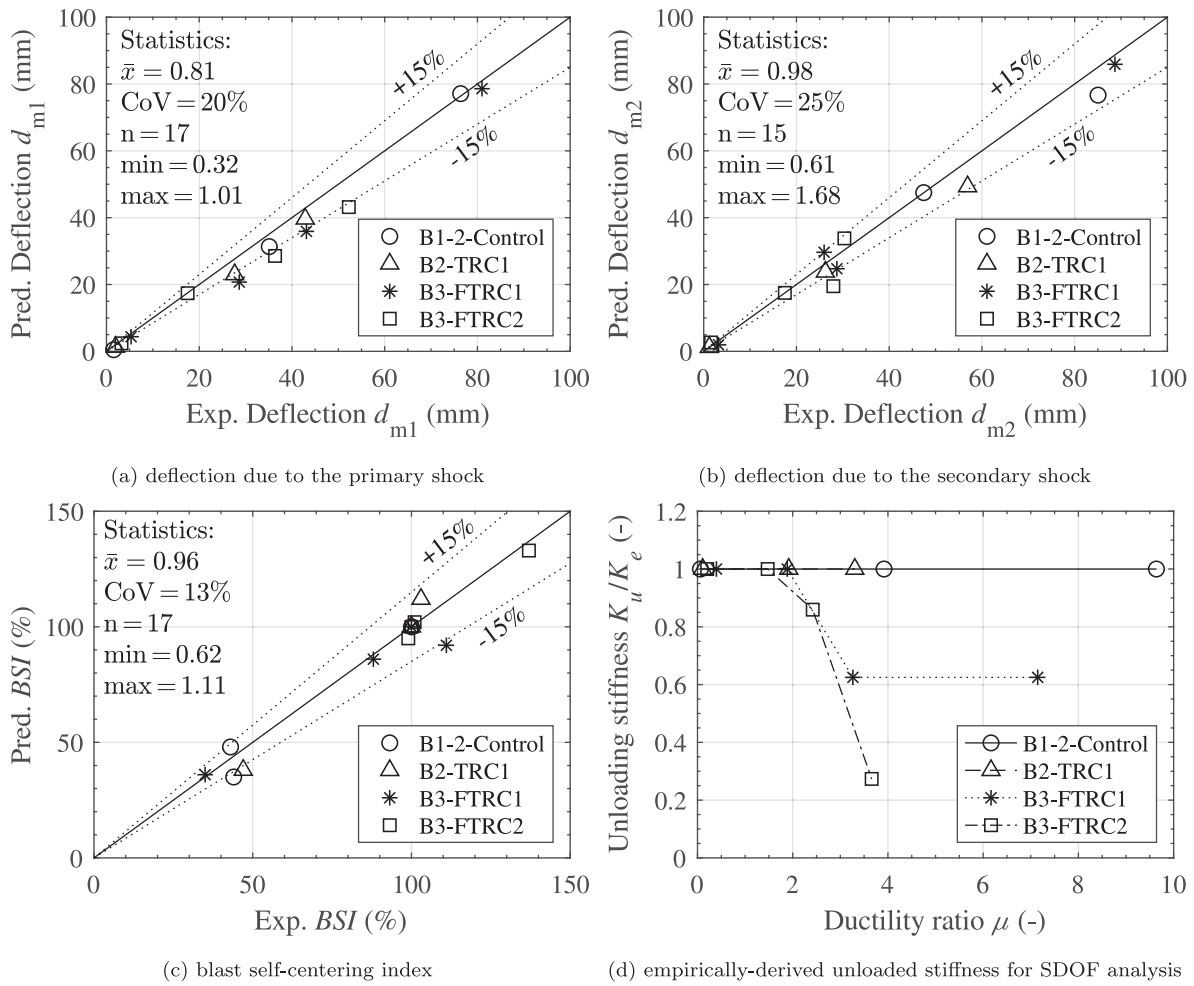
(a) deflection due to the primary shock

(b) deflection due to the secondary shock

(c) blast self-centering index

(d) empirically-derived unloaded stiffness for SDOF analysis

Fig. 13. Statistical summary of experimental and predicted results.

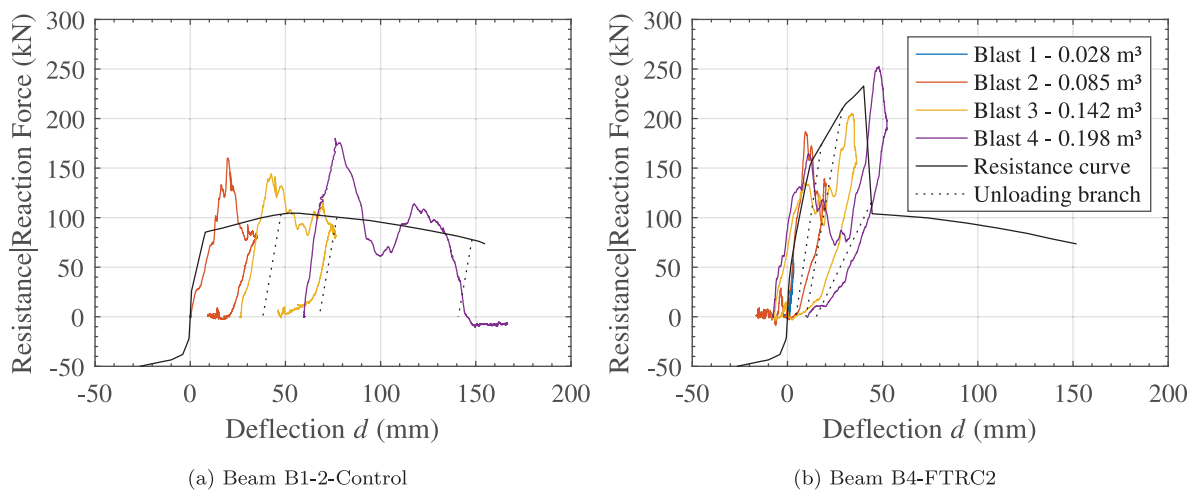(a) Beam B1-2-Control

(b) Beam B4-FTRC2

Fig. 14. Comparison of the analytical resistance function with inbound support reactions. (For interpretation of the references to color in this figure legend, the reader is referred to the web version of this article.)

are additive to the member resistance, leading to an increase in the magnitude of the support reaction beyond that predicted by a Biggs-type single degree of freedom idealization [50,51]. This phenomenon requires further investigation.

5. Conclusion

This work delves into the reinforcing potential of hybrid mineral-bonded strengthening layers incorporating textile grids and dispersed microfibers for improving the self-centering capacity of reinforced concrete (RC) beams subjected to increasing blast intensities. Five RC beams were produced, three of which were strengthened with a newly developed, sustainable fine-grained concrete. Various combinations of non-metallic reinforcement were incorporated into the mineral matrix. In particular, the effects of (i) the combination of short and continuous fiber reinforcement and (ii) the number of textile layers were investigated. A dynamic Single-Degree-of-Freedom (SDOF) analytical approach was employed to capture the complex response of the strengthened specimens and pave the way for accurate structural design provisions. The following main conclusions can be drawn:

- Both the control specimens and those retrofitted with textile-reinforced mineral-bonded composites failed at mid-span, with tensile rupture of the internal rebar and externally bonded carbon yarns. Conversely, the beams strengthened with hybrid reinforcement survived the blast sequence and showed residual load-bearing capacity, pointing out the crucial role of the synergistic action of the microfibers and the textile.
- In hybrid composites, the addition of short fibers to the matrix with high damage tolerance and strain capacity to embed the textile reinforcements provides the system with sufficient ductility to allow the full activation of the textile layers. In this way, the textiles can fully exert their reinforcing action. In fact, while the short fibers are key to governing the failure mode of the beam by smearing damage induced by the shock wave and optimizing the reinforcing action of the textile, the number of textile layers determines the load-bearing capacity and the residual deflection of the beam.
- Most remarkably, the crack-bridging capacity of the short fibers successfully prevents scabbing debris that cannot be inhibited by textile reinforcement alone. This entails significant positive implications for structural protection and human safety during extreme events.
- Nevertheless, it is observed that, regardless of the source of the blast and its direction of propagation, externally strengthened beams exhibit significant oscillations, which are also accentuated by the presence of the strengthening itself. This fact, albeit sought and well valued, emphasizes the need for additional reinforcement against rebound bending and cyclic loading. To this end, the proposal of a high ductility FTRC, as the one presented in this work, for the complete jacketing of concrete members is considered extremely promising to improve the structural performance against shock waves.
- SDOF modeling is performed using RCBlast and is shown to have good predictive capabilities even for extremely complex systems. The accuracy of the predictions, combined with the computational efficiency when compared to alternative numerical methods, like finite element analysis, makes SDOF viable for the analysis of similar scenarios and opens up good potential for optimizing the design of resilient structures.

In conclusion, it was found that thin hybrid reinforcing layers increase the toughness and damage tolerance of existing structural members and enhance the self-centering effects that are crucial for minimizing residual damage and retrofit costs. In addition, hybrid solutions appear to be much less susceptible to debonding failures as is often the case with FRP strengthening. This attribute further underscores their cost-effectiveness, making them a highly advantageous solution for long-term structural resilience and sustainability.

CRediT authorship contribution statement

Franz Bracklow: Writing – original draft, Visualization, Methodology, Investigation, Formal analysis, Data curation, Conceptualization. **Christopher M. Jackson:** Writing – original draft, Visualization, Validation, Software, Investigation, Formal analysis, Data curation. **Cesare Signorini:** Writing – review & editing, Writing – original draft, Visualization, Validation, Supervision, Project administration, Methodology, Investigation, Conceptualization. **Eric Jacques:** Writing – review & editing, Validation, Supervision, Software, Resources, Project administration, Methodology, Investigation, Funding acquisition, Conceptualization. **Birgit Beckmann:** Writing – review & editing, Supervision, Funding acquisition. **Manfred Curbach:** Writing – review & editing, Supervision, Funding acquisition. **Viktor Mechtcherine:** Writing – review & editing, Supervision, Funding acquisition.

Funding

Declaration of competing interest

The authors declare that they have no known competing financial interests or personal relationships that could have appeared to influence the work reported in this paper.

Acknowledgments

Appendix A. Complete experimental data

The results of the experimental campaign and how they compare with the analytical SDOF modelling are reported in full in Table A.3 and Table A.4.

Appendix B. Supplementary data

Supplementary material related to this article can be found online at https://doi.org/10.1016/j.engstruct.2024.119151.

Data availability

Data will be made available on request.

Table A.3
Summary of experimental blast test results.

Name	Blast	Primary shock				Secondary shock					Res.	Rot.	BSI
		P_{r1} (kPa)	I_{r1} (kPa ms)	d_{m1} (mm)	t_{m1} (ms)	P_{r2} (kPa)	I_{r2} (kPa ms)	t_a (ms)	d_{m2} (mm)	t_{m2} (ms)	d_r (mm)	θ_m (°)	(%)
B1-2-Control	1	8.9	12.8	1.6	12.7	3.4	7.7	69.7	1.6	67.1	0.0	0.1	100
	2	71.9	327.2	35.1	22.3	38.7	224.3	59.2	47.4	89.0	26.5	2.0	44
	3	78.9	391.8	76.4	23.9	44.4	221.7	59.2	85.0	82.5	59.9	3.5	43
	4	101.7	520.5	–	–	41.1	284.2	57.7	–	–	–	–	–
B2-TRC1	1	19.7	38.5	1.9	12.8	8.7	18.5	68.7	1.2	78.1	−0.8[a]	0.1	100
	2	72.9	351.7	27.7	18.8	34.9	211.2	59.3	26.2	82.4	−1.7	1.2	103
	3	78.4	402.8	42.9	30.0	39.6	241.7	58.5	56.9	85.5	29.3	2.4	47
	4	107.0	570.2	–	–	49.1	324.2	56.5	–	–	–	–	–
B3-FTRC1	1	37.2	97.6	5.3	23.8	16.1	45.5	64.5	3.2	63.9	1.8[a]	0.2	100
	2	74.5	343.9	28.6	18.5	40.4	220.1	58.5	28.7	79.9	−1.2	1.2	111
	3	78.2	385.2	43.1	21.3	30.0	177.4	58.7	26.0	89.0	4.0	1.8	88
	4	104.7	534.7	81.0	25.2	41.9	320.2	56.8	88.7	83.4	59.3	3.7	35
B4-FTRC2	1	28.8	61.6	3.2	10.8	14.1	26.8	67.7	1.6	42.5	−0.6[a]	0.1	100
	2	68.1	305.1	17.5	11.7	34.4	188.9	59.8	17.5	78.5	−7.3	0.7	137
	3	84.0	444.9	36.4	19.9	32.8	249.1	58.4	28.0	86.6	−7.7	1.5	101
	4	101.2	521.3	52.3	21.1	35.2	291.1	57.9	30.3	90.2	−7.1	2.2	99

[a] d_r is attributed e.g. to support settlement rather than flexural behavior. The value is assumed to be 0 for the BSI calculation.

Table A.4
Summary of SDOF analytical test results.

Name	Blast	Experimental results				Predicted results				Comparison pred./exp.			
		d_{m1} (mm)	d_{m2} (mm)	d_r (mm)	BSI (%)	d_{m1} (mm)	d_{m2} (mm)	d_r (mm)	BSI (%)	d_{m1} (–)	d_{m2} (–)	d_r (–)	BSI (–)
B1-2-Control	1	1.6	1.6	0.0	100	0.5	0.0	0.0	100	0.32	–	–	1.00
	2	35.1	47.4	26.5	44	31.3	47.5	30.8	35	0.89	1.00	1.16	0.80
	3	76.4	85.0	59.9	43	77.1	76.7	55.0	48	1.01	0.90	0.92	1.11
	4	–	–	–	–	Rupture of tensile reinf.				–	–	–	–
B2-TRC1	1	1.9	1.2	0.0	100	1.3	1.2	0.0	100	0.67	1.02	–	1.00
	2	27.7	26.2	−1.7	103	23.0	23.8	−3.0	112	0.83	0.91	1.71	1.09
	3	42.9	56.9	29.3	47	39.7	49.3	29.3	38	0.93	0.87	1.00	0.81
	4	–	–	–	–	Rupture of textile & reinf.				–	–	–	–
B3-FTRC1	1	5.3	3.2	0.0	100	4.4	2.0	−1.3	100	0.82	0.61	−0.73	1.00
	2	28.6	28.7	−1.2	111	20.7	24.7	0.7	92	0.72	0.86	−0.57	0.83
	3	43.1	26.0	4.0	88	35.9	29.7	5.5	86	0.83	1.14	1.38	0.98
	4	81.0	88.7	59.3	35	78.6	85.9	56.6	36	0.97	0.97	0.95	1.05
B4-FTRC2	1	3.2	1.6	0.0	100	2.4	2.7	−0.8	100	0.74	1.68	1.36	1.00
	2	17.5	17.5	−7.3	137	17.4	17.5	−6.8	133	0.99	1.00	0.94	0.97
	3	36.4	28.0	−7.7	101	28.6	19.5	−7.6	102	0.79	0.70	0.99	1.01
	4	52.3	30.3	−7.1	99	43.2	33.8	−4.9	95	0.83	1.11	0.69	0.96

References

[1] Draganić H, Gazić G, Varevac D. Experimental investigation of design and retrofit methods for blast load mitigation–a state-of-the-art review. Eng Struct 2019;190:189–209. http://dx.doi.org/10.1016/j.engstruct.2019.03.088.

[2] Goswami A, Adhikary SD. Retrofitting materials for enhanced blast performance of structures: Recent advancement and challenges ahead. Constr Build Mater 2019;204:224–43. http://dx.doi.org/10.1016/j.conbuildmat.2019.01.188.

[3] American Society of Civil Engineers. Structural design for physical security: state of the practice. Technical report, Reston, VA: ASCE Structural Engineering Institute; 2021, http://dx.doi.org/10.1061/9780784415498.

[4] Johnson J, Xu M, Jacques E. Predicting the self-centering behavior of hybrid FRP-steel reinforced concrete beams under blast loading. Eng Struct 2021;247:113117. http://dx.doi.org/10.1016/j.engstruct.2021.113117.

[5] Johnson J, Xu M, Jacques E. Self-centering hybrid GFRP-steel reinforced concrete beams for blast resilience. J Struct Eng 2021;147(7):04021099. http://dx.doi.org/10.1061/(ASCE)ST.1943-541X.0003019.

[6] Anas S, Alam M, Umair M. Experimental and numerical investigations on performance of reinforced concrete slabs under explosive-induced air-blast loading: A state-of-the-art review. Structures 2021;31:428–61. http://dx.doi.org/10.1016/j.istruc.2021.01.102.

[7] Alaedini S, Kabir MZ, Hejabi H. Seismic ductility evaluation of shear-deficient RC frames strengthened by externally bonded CFRP sheets. KSCE J Civ Eng 2016;20:1925–35. http://dx.doi.org/10.1007/s12205-015-0790-5.

[8] Koutas LN, Tetta Z, Bournas DA, Triantafillou TC. Strengthening of concrete structures with textile reinforced mortars: State-of-the-art review. J Compos Constr 2019;23(1):03118001. http://dx.doi.org/10.1061/(ASCE)CC.1943-5614.0000882.

[9] Koutas LN, Papakonstantinou CG. Flexural strengthening of RC beams with textile-reinforced mortar composites focusing on the influence of the mortar type. Eng Struct 2021;246:113060. http://dx.doi.org/10.1016/j.engstruct.2021.113060.

[10] Silva PF, Lu B. Improving the blast resistance capacity of RC slabs with innovative composite materials. Composites B 2007;38(5–6):523–34. http://dx.doi.org/10.1016/j.compositesb.2006.06.015.

[11] Wu C, Oehlers D, Rebentrost M, Leach J, Whittaker A. Blast testing of ultra-high performance fibre and FRP-retrofitted concrete slabs. Eng Struct 2009;31(9):2060–9. http://dx.doi.org/10.1016/j.engstruct.2009.03.020.

[12] Muszynski LC, Purcell MR. Composite reinforcement to strengthen existing concrete structures against air blast. J Compos Const 2003;7(2):93–7. http://dx.doi.org/10.1061/(ASCE)1090-0268(2003)7:2(93).

[13] Kadhom B, Almansour H, Saatcioglu M. Post-blast axial capacity of CFRP strengthened RC columns. In: IOP conference series: materials science and engineering. vol. 737, IOP Publishing; 2020, 012042. http://dx.doi.org/10.1088/1757-899X/737/1/012042.

[14] Jacques E, Lloyd A, Imbeau P, Palermo D, Quek J. GFRP-retrofitted reinforced concrete columns subjected to simulated blast loading. J Struct Eng 2015;141(11):04015028. http://dx.doi.org/10.1061/(ASCE)ST.1943-541X.0001251.

[15] Maazoun A, Matthys S, Belkassem B, Atoui O, Lecompte D. Experimental study of the bond interaction between CFRP and concrete under blast loading. Compos Struct 2021;277:114608. http://dx.doi.org/10.1016/j.compstruct.2021.114608.

[16] Jackson CM, Jacques E, Saatcioglu M. Blast retrofit of one-way reinforced concrete members using externally bonded FRP and FRP anchorage. Int J Prot Struct 2022;13(2):209–35. http://dx.doi.org/10.1177/20414196221087347.

[17] Ahmed A, Kodur V. The experimental behavior of FRP-strengthened RC beams subjected to design fire exposure. Eng Struct 2011;33(7):2201–11. http://dx.doi.org/10.1016/j.engstruct.2011.03.010.

[18] Ahmed MT, Jacques E. Strength and ductility of concrete confined by fiber metal laminate composites. J Mater Civ Eng 2024;36(6):04024110. http://dx.doi.org/10.1061/JMCEE7.MTENG-16814.

[19] American Concrete Institute. ACI 440.2R-17: Guide for the design and construction of externally bonded frp systems for strengthening concrete structures. ACI 440.2R-17, 2017.

[20] European Committee for Standardization. Eurocode 2: Design of concrete structures - part 1-1: General rules and rules for buildings; german version EN 1992-1-1:2004 + AC:2010. 2011-01, http://dx.doi.org/10.31030/1723945.

[21] Rossi E, Randl N, Harsányi P, Mészöly T. Experimental study of fibre-reinforced TRC shear strengthening applications on non-stirrup reinforced concrete T-beams. Eng Struct 2022;256:113923. http://dx.doi.org/10.1016/j.engstruct.2022.113923.

[22] Liu S, Zhu D, Li G, Yao Y, Ou Y, Shi C, Du Y. Flexural response of basalt textile reinforced concrete with pre-tension and short fibers under low-velocity impact loads. Constr Build Mater 2018;169:859–76. http://dx.doi.org/10.1016/j.conbuildmat.2018.02.168.

[23] Yang L, Xie H, Fang S, Huang C, Yang A, Chao YJ. Experimental study on mechanical properties and damage mechanism of basalt fiber reinforced concrete under uniaxial compression. Structures 2021;31:330–40. http://dx.doi.org/10.1016/j.istruc.2021.01.071.

[24] Tawfik A, Signorini C, Mechtcherine V. Direct assessment of the shear behavior of strain-hardening cement-based composites under quasi-static and impact loading: Influence of shear span and notch depth. Cem Concr Compos 2023;140:105119. http://dx.doi.org/10.1016/j.cemconcomp.2023.105119.

[25] Figueiredo TCS, Hering M, Curosu I, Bracklow F, Scheerer S, Curbach M, Mechtcherine V, de Andrade Silva F. Effect of shear reinforcement and external strengthening with strain-hardening cement-based composites (SHCC) on the impact resistance of reinforced concrete beams. Cem Concr Compos 2024;145:105371. http://dx.doi.org/10.1016/j.cemconcomp.2023.105371.

[26] Li B, Xiong H, Jiang J, Dou X. Tensile behavior of basalt textile grid reinforced engineering cementitious composite. Composites B 2019;156:185–200. http://dx.doi.org/10.1016/j.compositesb.2018.08.059.

[27] Ibrahim AM, Abd SM, Hussein OH, Tayeh BA, Najm HM, Qaidi S. Influence of adding short carbon fibers on the flexural behavior of textile-reinforced concrete one-way slab. Case Stud Constr Mater 2022;17:e01601. http://dx.doi.org/10.1016/j.cscm.2022.e01601.

[28] Signorini C, Bracklow F, Hering M, Butler M, Leicht L, Schubert T, Beigh MA, Beckmann B, Curbach M, Mechtcherine V. Ballistic limit and damage assessment of hybrid fibre-reinforced cementitious thin composite plates under impact loading. J Build Eng 2023;80:108037. http://dx.doi.org/10.1016/j.jobe.2023.108037.

[29] Hering M, Bracklow F, Scheerer S, Curbach M. Reinforced concrete plates under impact load—damage quantification. Materials 2020;13(20):4554. http://dx.doi.org/10.3390/ma13204554.

[30] Batarlar B, Hering M, Bracklow F, Kühn T, Beckmann B, Curbach M. Experimental investigation on reinforced concrete slabs strengthened with carbon textiles under repeated impact loads. Struct Concr 2021;22(1):120–31. http://dx.doi.org/10.1002/suco.201900319.

[31] Jacques E. Rcblast (version 0.5.1). 2014, URL: www.rcblast.ca.

[32] for Standardization EC. Concrete - specification, performance, production and conformity; German version EN 206:2013+a2:2021. 2021-06, http://dx.doi.org/10.31030/3198971.

[33] Antoni M, Rossen J, Martirena F, Scrivener K. Cement substitution by a combination of metakaolin and limestone. Cem Concr Res 2012;42(12):1579–89. http://dx.doi.org/10.1016/j.cemconres.2012.09.006.

[34] Sharma M, Bishnoi S, Martirena F, Scrivener K. Limestone calcined clay cement and concrete: A state-of-the-art review. Cem Concr Res 2021;149:106564. http://dx.doi.org/10.1016/j.cemconres.2021.106564.

[35] Ahmed AH, Nune S, Liebscher M, Köberle T, Willomitzer A, Noack I, Butler M, Mechtcherine V. Exploring the role of dilutive effects on microstructural development and hydration kinetics of limestone calcined clay cement (LC^3) made of low-grade raw materials. J Clean Prod 2023;428:139438. http://dx.doi.org/10.1016/j.jclepro.2023.139438.

[36] FibrXL. UHMWPE dyneema fiber - product data sheet. 2020, URL: https://fibrxl.com/wp-content/uploads/2020/07/FibrXL-PDS-performance-0720-DEF-Dyneema.pdf.

[37] Wilhelm Keitz Solutions in Textile GmbH. Technical data sheet: Sitgrid040ki. 2020.

[38] Kaufmann N. Das Sandflächenverfahren. Ein einfaches Verfahren zur Messung und Beurteilung der Textur von Fahrbahnoberflächen. Straßenbautechnik 24(3):131–5, 1071.

[39] Lloyd A, Jacques E, Saatcioglu M, Palermo D, Nistor I, Tikka T. Capabilities of a shock tube to simulate blast loading on structures. ACI Special Publ 2011;281:1–20. http://dx.doi.org/10.14359/51683611.

[40] Burrell RP, Aoude H, Saatcioglu M. Response of SFRC columns under blast loads. J Struct Eng 2015;141(9):04014209. http://dx.doi.org/10.1061/(ASCE)ST.1943-541X.0001186.

[41] Aoude H, Dagenais FP, Burrell RP, Saatcioglu M. Behavior of ultra-high performance fiber reinforced concrete columns under blast loading. Int J Impact Eng 2015;80:185–202. http://dx.doi.org/10.1016/j.ijimpeng.2015.02.006.

[42] Crawford JE. State of the art for enhancing the blast resistance of reinforced concrete columns with fiber-reinforced plastic. Can J Civil Eng 2013;40(11):1023–33. http://dx.doi.org/10.1139/cjce-2012-0510.

[43] Jacques E. Blast retrofit of reinforced concrete walls and slabs. (Ph.D. thesis), Ottawa: University of Ottawa; 2011, http://dx.doi.org/10.20381/ruor-4448.

[44] Kent DC, Park R. Flexural members with confined concrete. J Struct Div 1971;97(7):1969–90. http://dx.doi.org/10.1061/JSDEAG.0002957.

[45] International Federation for Structural Concrete (fib). fib Model code for concrete structures 2010 Ernst & Sohn; 2013, http://dx.doi.org/10.35789/fib.BULL.0055.

[46] Scott BD, Park R, Priestley MJ. Stress-strain behavior of concrete confined by overlapping hoops at low and high strain rates. In: Journal proceedings vol. 79, 1982, p. 13–27. http://dx.doi.org/10.14359/10875.

[47] Malvar LJ. Review of static and dynamic properties of steel reinforcing bars. Mater J 1998;95(5):609–16. http://dx.doi.org/10.14359/403.

[48] Yalcin C, Saatcioglu M. Inelastic analysis of reinforced concrete columns. Comput Struct 2000;77(5):539–55. http://dx.doi.org/10.1016/S0045-7949(99)00228-X.

[49] Biggs JM. Introduction to structural dynamics McGraw-Hill; 1964.

[50] Ardila-Giraldo OA. Investigation on the initial response of beams to blast and fluid impact (Ph.D. thesis), Purdue University; 2010, URL: https://docs.lib.purdue.edu/dissertations/AAI3417989/.

[51] Adaros MS, Wood S, Van Eepoel P. Effect of inertia forces on support reactions of beams subjected to uniform blast loads. In: Structures congress 2013: bridging your passion with your profession 2013, p. 93–102. http://dx.doi.org/10.1061/9780784412848.009.